Electronic Supplementary Material (ESI) for ChemComm.

Potassium Nitrilotriacetate as Multi-functional Buried Interface Modifier for Hysteresis-reduced Perovskite Solar Cells

Meiling Yang[a], Gaoyi Han[a*], Wenjing Hou[a*], Yaoming Xiao[a,b*]

[a] Institute of Molecular Science, Key Laboratory of Chemical Biology and Molecular Engineering of Education Ministry, Key Laboratory of Materials for Energy Conversion and Storage of Shanxi Province, State Key Laboratory of Quantum Optics and Quantum Optics Devices, Shanxi University, Taiyuan 030006, P. R. China.

[b] College of Chemical Engineering and Materials Science, Quanzhou Normal University, Quanzhou 362000, P. R. China.

[*] Corresponding authors.

E-mail: houwenjing@sxu.edu.com (Wenjing Hou); han_gaoyis@sxu.edu.cn (Gaoyi Han); ymxiao@qztc.edu.cn (Yaoming Xiao)

Material:

The ITO glass substrates were purchased from the Kunshan Sunlaite New Energy Technology co., LTD. The SnO_2 colloid dispersion (15 wt.% in H_2O) and 4-tert-butylpyridine (tBP, 96%) were from Alfa Aesar. Lead iodide ($PbI_2 \geq 99.99\%$), 2,2',7,7'-tetrakis[N,N-di-(4-Methoxyphenyl)amino]-9,9'-spirobifluorene, (Spiro-OMeTAD≥99.8%), Cesium iodide (CsI, 99.9%) and CH_3NH_3Cl (MACl, 99.5%) were purchased from Xi'an Polymer Light Technology Corp. Ltd. CH_3NH_3I (MAI), $HC(NH_2)_2I$ (FAI), and CH_3NH_3Br (MABr) were bought from Greatcell Solar

Materials Pty Ltd; Acetonitrile (ACN ≥ 99.9%) was brought from Aladdin chemistry Co. Ltd. Anhydrous 2-propanol (IPA, 99.5%), N,N-dimethylformamide (DMF, 99.8%), dimethyl sulfoxide (DMSO ≥ 99.9%), chlorobenzene (CB, 99.8%) and bis (trifluoromethane) sulfonimide lithium salt (LiTFSI ≥99.0%) were purchased from Sigma. Aldrich, Corp. Ltd. Nitrilotriacetic acid (NTA) was purchased Tianjing Chemical Reagent No.1 plant. KOH was obtained from Tianjing HengXing Chemical Reagent Co. Ltd. All chemicals and reagents were used as received without further purification.

Device Fabrication:

The ITO glasses were sequentially ultrasonic cleaned with abluent, deionized water and ethanol for 30 min, respectively. After drying under a flow of N_2, the ITO glass substrates were transferred into a UV-Ozone cleaner for 45 min to remove the residual organics and improve the work function of ITO glass substrates. The devices were fabricated on the above treated ITO glass substrates by spin-coating methods. First, the diluted SnO_2 colloidal solution with deionized water (volume rate 1:5) was spin-coated onto clean ITO glass substrates in ambient air with a spin rate of 3000 rpm for 30 s and annealed on a hot plate at 150 °C for 30 min. After cooling to room temperature, the ITO/SnO_2 films were processed with UV-ozone treatment for 45 min. Then, the pammonium triacetate (NTA) was dissolved in potassium hydroxide solution with different concentration (0.00 mM, 0.50 mM, 0.75 mM and 1.00 mM) to form potassium ammonium triacetate (NTAK). The NTAK solution was spun onto the SnO_2 at a speed of 3000 rpm for 30 s, and heated on a hot plate at 120 °C for 15

min. Next, the perovskite films were deposited using two-step sequential deposition in the argon-filled glove box. First, the hot PbI_2 solution (1.3 M PbI_2 and 3 wt% CsI in V_{DMF}/V_{DMSO}= 9:1) was spun onto the ITO/SnO_2/NTAK films at 2500 rpm for 30 s and heated at 70 °C for 1 min in the glove box. Next, the mixed organic amine solution (0.12 M MAI, 0.05 M MABr, 0.03 M MACl and 0.23 M FAI dissolved in IPA) was spun onto PbI_2 films at 2300 rpm for 30 s and the samples were transferred from the glove box to heat on a hot plate at 150 °C for 15 min in air atmosphere. After the substrates were cooled down to room temperature, the hole transport layer of spiro-OMeTAD was spin-coated at 3000 rpm for 30 s, which was prepared by dissolving 75 mg of Spiro-OMeTAD, 35 μL Li-TFSI solution (260 mg mL^{-1} in acetonitrile) and 30 μL of 4-tert-butypyridine in 1 mL chlorobenzene. Finally, Ag was thermally evaporated in a vacuum to form the electrode.

Characterizations:

The absorption and optical transmission spectra of the perovskite films were examined by the thermo scientific evolution 220 UV-visible spectrophotometer. The crystallinity of the perovskite films was analyzed through the X-ray powder diffraction by BRUKER D8-ADVANCE with the Cu Kα radiation source (λ=1.5418Å) and the working voltage of 40 kV and working current of 40 mA, respectively. X-ray photoelectron spectroscopy (XPS, Kratos Analytical Ltd AXIS ULTRA) profiles were measured with a monochromic Al Kα source at 1486.6 eV. Considering the non-exposed feature of buried perovskite interfaces, the NTAK solution was deposited on the surface of as-prepared PbI_2 film to study the interaction between NTAK and perovskite indirectly. The field emission scanning electron microscopy with the working voltage of 10 kV (FESEM, JEOL-JSM-6701F) was employed to observe the top and cross-sectional characteristics. The energy dispersive

X-ray spectroscopy (EDS) attaching to the FESEM was employed to verify the distribution of chemical compositions in samples. The J-V curves are measured under the dark condition with reverse scan direction from -0.5 V to 1.5 V by CHI660E workstation. The space charge limited current (SCLC) testing was verified by linear cyclic voltammetry method of CHI660E workstation with the scan rate of 0.1 V s^{-1} from 0 to 1 V. The steady state photoluminescence (PL) curves were carried out using confocal raman systems (iHR 550 HORIBA) with laser of 532 nm. The time-resolved fluorescence spectra obtained by a home-built scanning confocal system based on an invert microscope (Nikon, TE2000-U) in State Key Laboratory of Quantum Optics and Quantum Optics Devices of Shanxi University. Ultraviolet photoelectron spectroscopy (UPS, Thermo ESCALAB XI+) were measured with a monochromatic He I light source (21.22 eV) and a VG Scienta R4000 analyzer. A sample bias of -5 V was applied to observe the secondary electron cutoff (SEC). The external quantum efficiencies (EQE, Zennium CIMPS-pcs2 (Zahner)) was measured with the tunable light source (TLS03). The current density versus voltage (J-V) test and light intensity dependence curves were conducted under illumination by a solar simulator (CEL-AAAS50) assembled with a Keithley 2400 source meter. J□V curves were generated using a solar simulator and a Keithley 2400 source meter. The light intensity was calibrated using a light irradiation meter and a standard Si photovoltaic cell. The J-V curves were measured from 0 V to 1.2 V (forward scan) or from 1.2 V to 0 V (reverse scan) with a scan rate of 100 mV s^{-1}. The size of the active area of the devices was defined to be 0.1 cm^2 by using a metal mask. The time-dependent density functional theory (DFT) theoretical calculation was performed using the Guassian program package to calculate and visualize the electrostatic potential (ESP) maps of NTAK employing B3LYP/6-31G(d) level. The electrochemical impedance spectra (EIS) and Mott-Schottky curve were recorded on a CHI660E electrochemical workstation with a frequency of 10^6 Hz in the dark state. Mott-Schottky curve at 1000 Hz of the devices based on SnO_2 and SnO_2 modified by NTAK. Time-of-flight secondary ion mass spectrometry (TOF-SIMS) was measured by using a dual-beam TOF-SIMS IV (IONTOF) spectrometer equipped with a 30 keV, 1pA Bi^{3+} beam for the analysis and

a 1 KeV, 1nA O^{2-} ion beam for the sputtering operated in noninterlaced mode. Liquid Ultraviolet-visible (UV-vis) spectra were recorded on U-3900 UV-Visible spectrophotometer. The un-encapsulated devices for stability measurement were aged at 25 °C in dark moisture-proof box with the humidity of 1%-2% RH and in dark air condition with the humidity of 10%-20% RH. And the values presented in stability measurement are the average values of at least 20 devices.

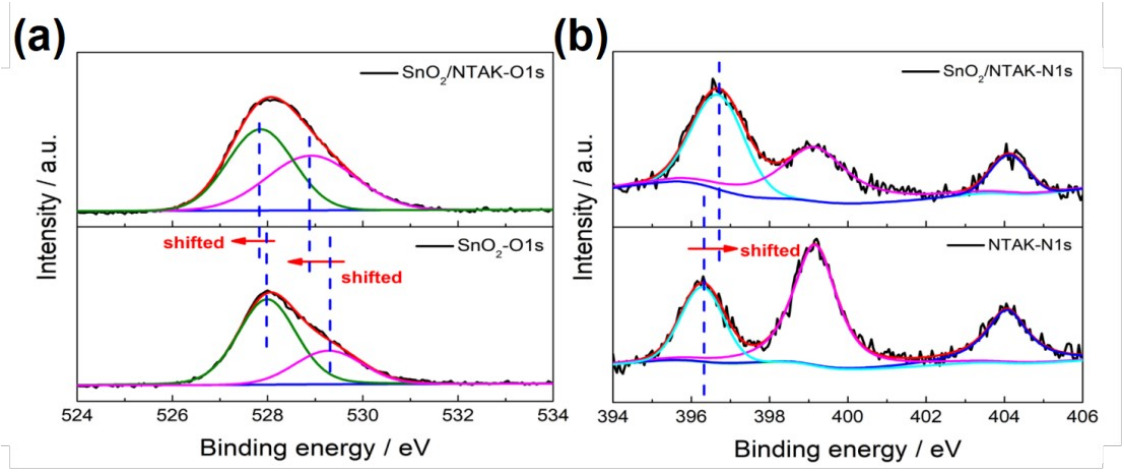

Fig. S1 XPS spectra of SnO_2, NTAK and NTAK modified SnO_2: (a) O 1s and (b) N 1s.

In Fig.S1a, the NTAK modification also makes the XPS peak of lattice oxygen at 527.99 eV and chemisorbed hydroxyl oxygen at 529.30 eV shifting to 527.83 eV and 528.91 eV, respectively. In **Fig. S1b**, the characteristic peak of $-(CH_2)_3N$ in NTAK is located at 396.32 eV, which shifts to 396.72 eV after interacting with SnO_2. The decreased binding energy of O 1s revealed that the SnO_2 can obtain electrons from NTAK, which can be ascribed to that the $-COO^-$ can link to the lattice oxygen and -OH on SnO_2 preferentially. The increased binding energy of N1s for $-(CH_2)_3N$ can be ascribed to that the N can donate its lone pair electrons by forming hydrogen bond with the -OH on SnO_2.

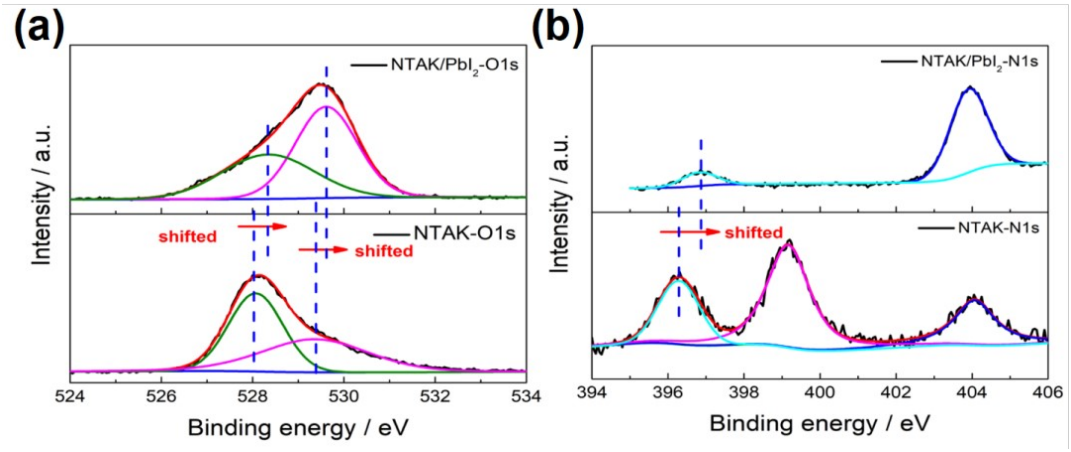

Fig. S2 XPS spectra of NTAK and NTAK modified PbI_2 : (a) O 1s and (b) N 1s.

The carboxyl O (528.06 eV) and ester O (529.39 eV) in NTAK all shift to the higher binding energy of 528.32 eV and 529.61 eV, respectively. The characteristic peak of $-(CH_2)_3N$ for NTAK also shifts from 396.32 eV to higher binding energy of 396.88 eV.

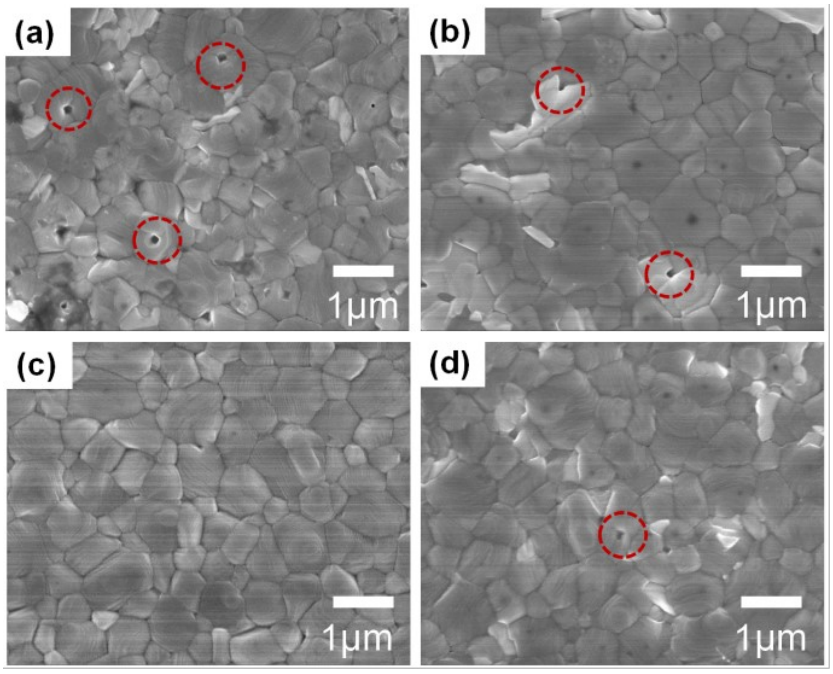

Fig. S3 Top FESEM images of the perovskite films deposited on SnO_2 with different concentration of NTAK modification: (a) 0.00 mM, (b) 0.05 mM, (c) 0.75 mM, and (d) 1.00 mM, respectively.

The morphology of perovskite film is one of the key factors affecting the device

performances. In Fig.S3, with the increase of NTAK concentration, the morphologies of the perovskite films change significantly. And the number of pinhole at the surface of perovskite reduced with the NTAK concentration increased from 0 mM to 0.75 mM (Fig. S3a-c). When the concentration of NTAK was 0.75 mM, the morphology of the film was improved significantly (Fig. S3c), which can be attributed to that the NTAK can coordinate with the PbI_2 to retard the crystallization rate of perovskite. However, with the concentration of NTAK further increased (1.0 mM), the number pinhole of the film was increased (Fig. S3d). So, excessive NTAK could influence the device performances by affecting the quality of the perovskite film.

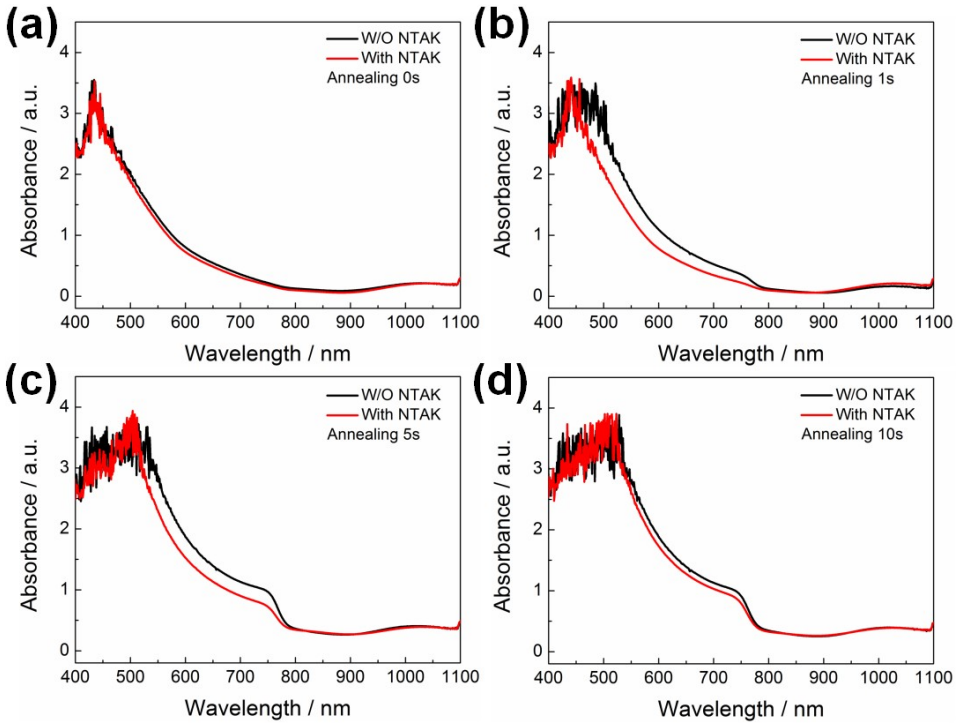

Fig. S4 UV-vis absorption spectra of perovskite films based on the ITO/SnO_2 substrates without and with NTAK modification with different annealing time: (a) 0 s, (b) 1 s, (c) 5 s, and (d) 10 s , respectively.

We have proved that NTAK can coordinate with the PbI_2 to retard the crystallization rate of perovskite by testing the UV-vis absorption spectra of perovskite films with different annealing time based on the ITO/SnO_2 substrates without or with NTAK modification. In order to avoid the influence of film thickness on the absorbance of perovskite film, we control the concentration of precursor solution and spin-coating speed completely consistent. As shown in Fig. S4a, the

absorbance intensity of the initial perovskite films have no obvious differences. After annealing for several seconds, the perovskite film based on the ITO/SnO_2 substrates with NTAK modification exhibits the lower absorbance than that without NTAK modification, especially for the perovskite film annealed for 1s and 5s. The lower absorbance can reveal that the perovskite with NTAK modification has a slower crystallization rate. Therefore, we think that NTAK can coordinate with the PbI_2 to retard the crystallization rate of perovskite.

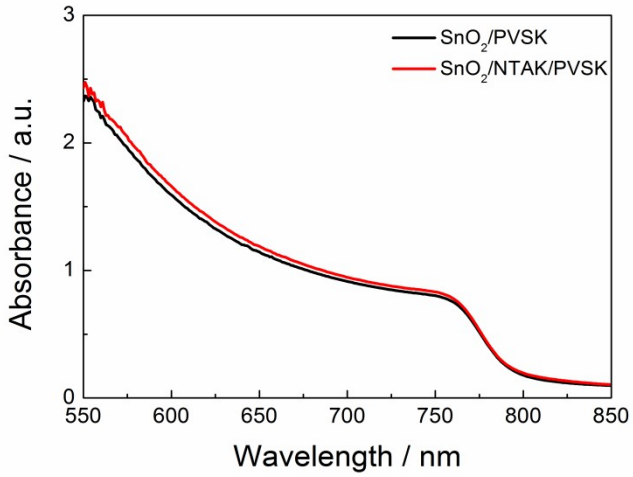

Fig. S5 UV−vis absorption spectra of the perovskite films deposited on SnO_2 substrates W/O or with NTAK modification.

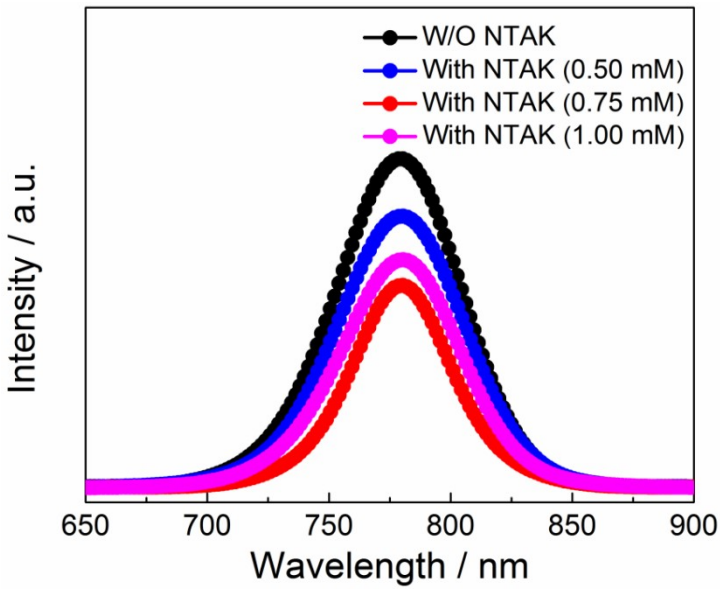

Fig. S6 Steady-state PL spectra of the perovskite films deposited on SnO_2 with various concentration of NTAK modification.

According to Steady-state PL spectra in Fig. S6, with the increase of NTAK concentration from 0 to 1.0 mM, the PL intensity was reduced successively. And when the concentration of NTAK was 0.75 mM, the perovskite film shows the most PL intensity quenching, which can be explained by the improved morphology and the least pinhole defects in Fig. 2d and Fig. S3. Compared with other conditions, the lowest PL intensity indicates that the perovskite film based on 0.75 mM NTAK modified SnO_2 shows the better interface charge extraction.

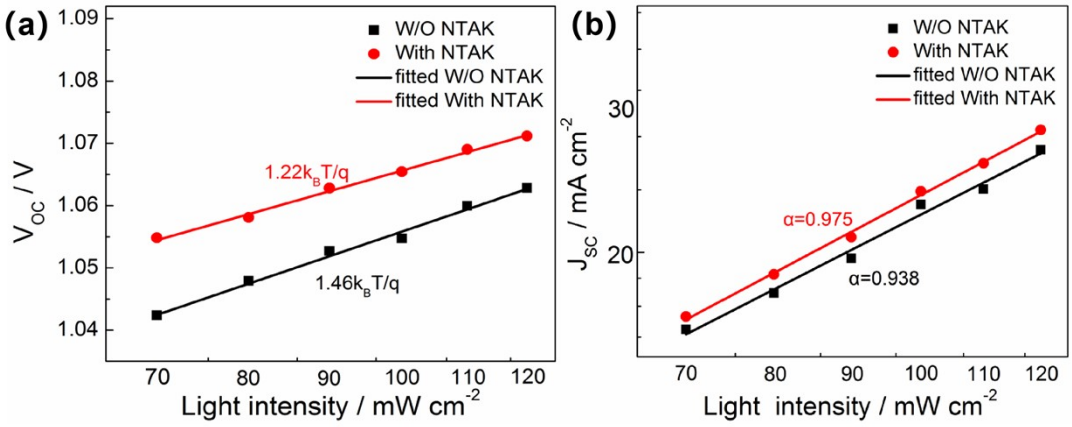

Fig. S7 Light intensity dependent (a) V_{OC} and (b) J_{SC} curves of devices based on the ITO/SnO_2 substrates W/O or with NTAK modification.

To explore the mechanism of charge recombination, we measured the J-V curves under different light intensity (I). In **Fig. S7a**, the light intensity and V_{OC} obey the following relationship：

$V_{OC}=(nk_BTln(I)/q)+A$

where k_B is the Boltzmann constant, T is the absolute temperature, q is the elementary charge, n is an ideal factor, and A is a constant. The smaller the slope indicates the lower possibility of trap-related recombination. The slope of the NTAK modified device decrease from 1.46 k_BT/q to 1.22 k_BT/q, which reveals that the nonradiative recombination is suppressed after the NTAK modification. In Fig. S7b, I and J_{SC} obey the following law: $J_{SC} \propto I^{\alpha}$, where α is an exponential factor. The α value of the NTAK-modified device is 0.975, being closer to 1 than α of 0.938 of the devices without NTAK, indicating that NTAK modification is contribute to carrier

transport.

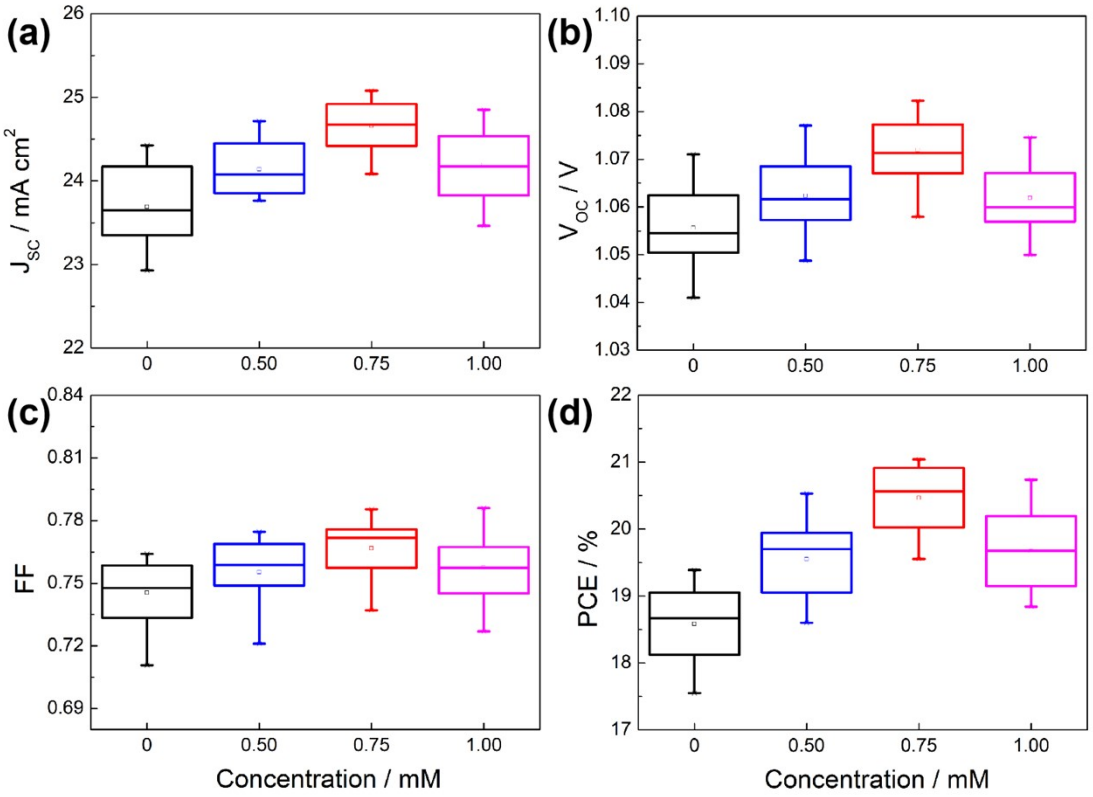

Figure S8. Statistical distribution diagram of the photovoltaic parameters for 20 PSCs based on SnO_2 with various concentrations of NTAK modification: (a) J_{SC}, (b) V_{OC}, (c) FF, and (d) PCE, respectively.

According to J-V characteristics curves and statistical distribution diagram of the photovoltaic parameters for PSCs (Fig. S8-S9), the PSC based on the 0.75 mM NTAK modified SnO_2 achieved the highest photovoltaic parameters than other conditions. After modified by 0.75 mM NTAK, the reduced defects and nonradiative recombination can be used to explain the improved device performances.

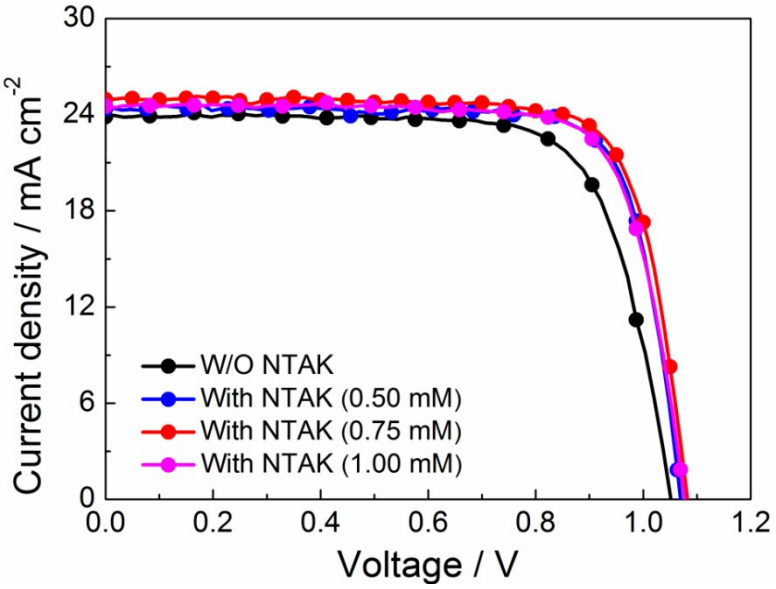

Fig. S9 J-V characteristics curves of the PSCs with various concentration of NTAK modification.

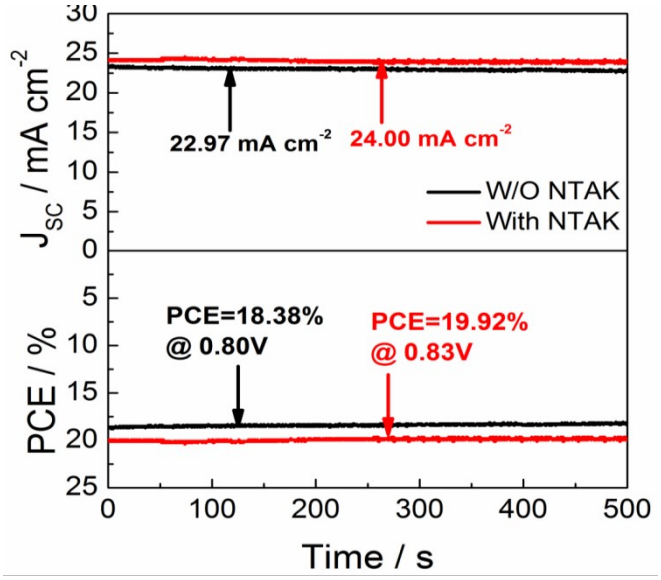

Fig. S10 Steady-state current density and PCE versus time for the best-performing devices without and with NTAK modification measured at the maximum power point.

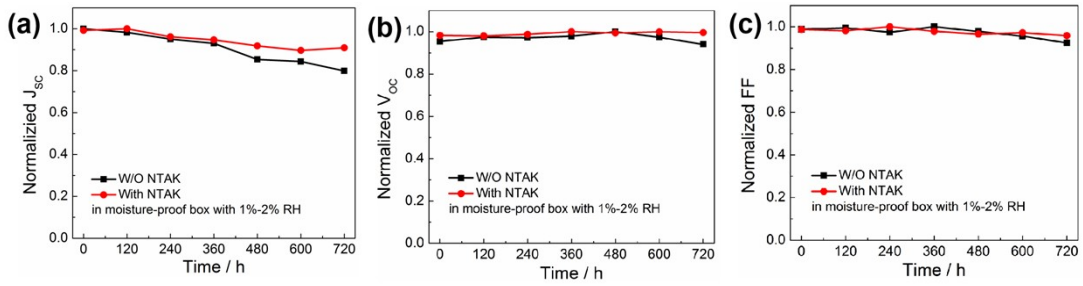

Fig. S11 Normalized (a) J_{SC}, (b) V_{OC}, and (c) FF as evaluation parameters for the unencapsulated devices based on SnO_2 W/O and with NTAK modification aged in moisture-proof box with the relative humidity of 1%-2% RH in the dark at the room temperature.

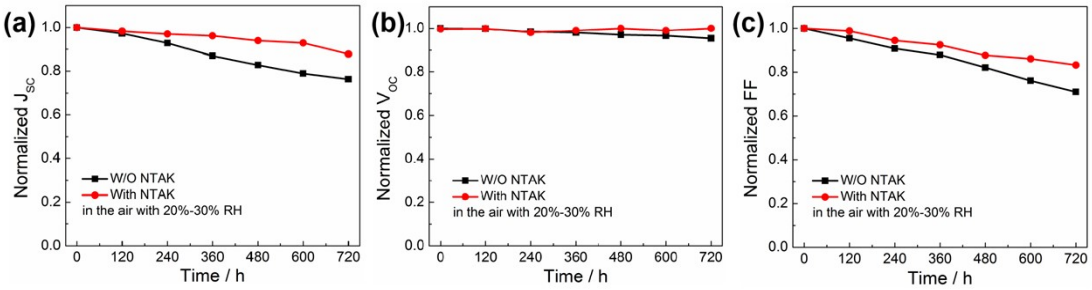

Fig. S12 Normalized (a) J_{SC}, (b) VOC, and (c) FF as evaluation parameters for the unencapsulated devices based on SnO_2 W/O and with NTAK modification aged in the air with relative humidity of 20%-30% RH in the dark at the room temperature.

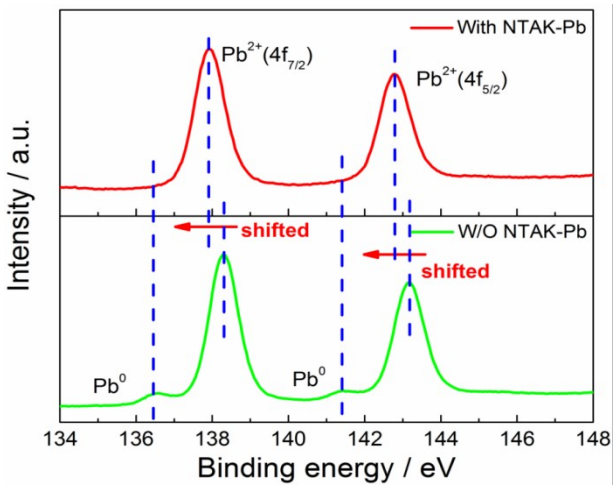

Fig. S13 X-ray photoelectron spectroscopy (XPS) of Pb 4f for the perovskite films without and with NTAK modification aged for 3 days.

Henry J. Snaith has proposed the mechanisms of I_2 generation: The I^- at lattice site and interstitial site capture hole, and then diffuse to combine for generating I_2. Therefore, the I_2 generation is the results of I^- migration, diffusion and be oxidized, accompanying with the reduction from Pb^{2+} to Pb^0. We measured the X-ray photoelectron spectroscopy (XPS) spectrum of the perovskite films without and with NTAK aged for 3 days. Besides of the peaks of Pb^{2+}, the perovskite film without NTAK contains the peaks of Pb^0 at 136.45 eV (Pb^0 $4f_{7/2}$) and 141.41 eV (Pb^0 $4f_{5/2}$) (Fig. S13). And the generation of Pb^0 is often accompanied with the processes of I^- migration, combine, and are oxidized to generate the I_2. After NTAK modification, the shifted Pb^{2+} peaks reveal that the NTAK can coordinate with uncoordinated Pb^{2+}. While the disappeared Pb^0 peak prove that the NTAK can suppress the I_2 generation by inhibiting the I^- migration. Therefore, we think that the I_2 generation in the toluene is related to I^- migration. And the related contents have been supplemented in the revised manuscript and supporting information.

Table S1. Energy level parameters of materials used in the device.

Sample	E_{cutoff}	$E_{F,edge}$ (eV)	E_{VB} (eV)	Eg (eV)	E_{CB} (eV)
W/O NTAK	17.41	4.31	-8.12	3.90	-4.22
With NTAK	17.94	4.79	-8.07	3.90	-4.17

Table S2. TRPL data of perovskite films deposited on SnO_2 W/O or with NTAK modification.

Sample	A_1	τ_1 (ns)	A_2	τ_2 (ns)	T_{ave} (ns)
W/O NTAK	0.66	4.97	0.34	69.46	61.73
With NTAK	0.54	10.23	0.46	38.52	31.88

Table S3. Averaged photovoltaic performances parameters of the 20 devices without and with NTAK modification measured in reverse scan.

Device	J_{SC} (mA cm^{-2})	V_{OC} (V)	FF (%)	η (%)
W/O NTAK	23.58±0.73	1.05±0.02	74.55±1.86	18.58±0.80
With NTAK	24.67±0.41	1.08±0.01	76.68±1.82	20.47±0.55

Table S4. Photovoltaic performances parameters of the best-performing devices without and with NTAK modification measured in reverse and forward scan under AM 1.5 G 1 sun illumination of 100 mW cm^{-2}.

Device	Scan direction	J_{SC} (mA cm^{-2})	V_{OC} (V)	FF (%)	η (%)	HI
W/O NTAK	RS	23.58	1.05	77.00	19.06	0.093
	FS	23.51	1.05	70.00	17.28	
With NTAK	RS	24.95	1.08	78.00	21.02	0.076
	FS	25.08	1.09	71.01	19.41	

Table S5 . Summary of photovoltaic performance of reported high-efficiency Cs-MA-FA-based PSCs in recent years.

Device structure	J_{SC} (mA/cm^2)	V_{OC} (V)	FF	PCE (%)	Active area (cm^2)	Ref.
ITO/SnO_2/NTAK/$(Cs_{0.05}FA_{0.54}MA_{0.41})Pb(I_{0.98}Br_{0.02})_3$/Spiro-OMeTAD/Ag	**24.95**	**1.08**	**0.78**	**21.02**	**0.1**	**This work**
FTO/SnO_2/$Cs_{0.05}(MA_{0.17}FA_{0.83)0.95}Pb(I_{0.83}Br_{0.17})_3$/Spiro-OMeTAD/Au	23.05	1.130	0.798	20.79	0.09	S1
ITO/Sb□SnO_2/$Cs_{0.05}(FA_{0.85}MA_{0.15})_{0.95}Pb(I_{0.85}Br_{0.15})_3$/Spiro-OMeTAD/Au	23.90	1.173	0.740	20.73	0.1	S2
FTO/Ru□SnO_2/$Cs_{0.05}(MA_{0.10}FA_{0.90})_{0.95}Pb(I_{0.90}Br_{0.10})_3$/Spiro-OMeTAD/Au	24.60	1.150	0.780	22.00	0.16	S3
FTO/Nb□SnO_2/$FA_{0.75}MA_{0.2}Cs_{0.05}Pb(I_{0.14}Br_{0.86})_3$/Spiro-OMeTAD/Au	22.77	1.157	0.747	20.47	0.16	S4
FTO/Y□SnO_2/$Cs_{0.05}(MA_{0.15}FA_{0.85})_{0.95}Pb(I_{0.85}Br_{0.15})_3$/Spiro-OMeTAD/Au	23.56	1.130	0.778	20.71	0.12	S5
FTO/Nd-SnO_2/$Cs_{0.05}(MA_{0.17}FA_{0.83})_{0.95}Pb(I_{0.83}Br_{0.17})_3$/Spiro-OMeTAD/Au	23.85	1.122	0.782	20.92	0.08	S6
ITO/SnO_2/$FA_{0.80}MA_{0.15}Cs_{0.05}PbI_{2.55}Br_{0.4}$/HABr/Spiro-OMeTAD/Au	23.70	1.230	0.810	23.60	0.0706	S7
ITO/SnO_2/SA/$Cs_{0.05}(FA_{0.85}MA_{0.15})_{0.95}Pb(I_{0.85}Br_{0.15})_3$/Spiro-OMeTAD/Au	22.80	1.150	0.779	20.41	No	S8
ITO/SnO_2/glycine/$Cs_{0.05}MA_yFA_{0.95-y}PbI_{3-x}Cl_x$/Spiro-OMeTAD/Ag	24.15	1.100	0.780	20.68	0.075	S9
FTO/SnO_2/$Cs_{0.05}(MA_{0.17}FA_{0.83})_{0.95}Pb(I_{0.83}Br_{0.17})_3$/Spiro-OMeTAD/Au	22.75	1.160	0.740	19.51	0.08	S10
FTO/TiOxNy/meso-TiO_2/PMMA:PCBM/$Cs_{0.05}FA_{0.9}MA_{0.05}PbI_{2.74}Br_{0.26}$ /PMMA/P_3HT:CuPc/Au	22.80	1.193	0.859	23.36	1	S11
ITO/(SnO_2-PEIE)/(PCBM/$MnSO_4$)/$MA_{0.10}Cs_{0.05}FA_{0.85}Pb(I_{0.95}Br_{0.05})_3$/PDCB/PTAA-BCF/Au	24.20	1.110	0.778	20.90	0.113	S12
FTO/TiO_2/SnO_2/(PbI_2:$PbBr_2$:FAI:MAI:CsI:MACl=0.98:0.02:0.81:0.04:0.05 :0.20)/$PDEAI_2$/Spiro-OMeTAD)/Au	24.75	1.160	0.835	23.92	0.09	S13

Reference:

S1 G. Yang, C. Chen, F. Yao, Z. Chen, Q. Zhang, X. Zheng, J. Ma, H. Lei, P. Qin, L. Xiong, W. Ke, G. Li, Y. Yan and G. Fang, *Adv. Mater*., 2018, 30, 1706023.

S2 Q. Cao, Z. Li, J. Han, S. Wang, J. Zhu, H. Tang, X. Li and X. Li, *Sol. RRL*, 2019, 3, 1900333.

S3 S. Akin, *ACS Appl. Mater. Interfaces*, 2019, 11, 39998–40005.

S4 E. Anaraki, A. Kermanpur, M. Mayer, L. Steier, T. Ahmed, S. Turren-Cruz, J. Seo, J. Luo, S. Zakeeruddin, W. Tress, T. Edvinsson, M. Grätzel, A. Hagfeldt and J. Correa-Baena, *ACS Energy Lett.*, 2018, 3, 773-778.

S5 J. Song, W. Zhang, D. Wang, K. Deng, J. Wu and Z. Lan, *Sol. Energy*, 2019, 185, 508-515.

S6 J. Jia, J. Dong, J. Wu, H. Wei and B. Cao, *J. Alloys Compd*., 2020, 844, 156032.

S7 S. Tang, J. Bing, J. Zheng, J. Tang, Y. Li, M. Mayyas, Y. Cho, T. Jones, T. Yang, L. Yuan, M. Tebyetekerwa, H. Nguyen, M. Nielsen, N. Ekins-Daukes, K. Kalantar-Zadeh, G. Wilson, D. McKenzie, S. Huang and A. Ho-Baillie, *Cell Rep. Phys. Sci.* 2021, 2, 100511.

S8 H. Xia, X. Li, J. Zhou, B. Wang, Y. Chu, Y. Li, G. Wu, D. Zhang, B. Xue, X. Zhang, Y. Hu, H. Zhou and Y. Zhang, *ACS Appl. Energy Mater.* 2020, 3, 3186-3192.

S9 J. Du, L. Feng, X. Guo, X. Huang, Z. Lin, J. Su, Z. Hu, J. Zhang, J. Chang and Y. Hao, *J. Power Sources*, 2020, 455, 227974.

S10 J. Ma, X. Zheng, H. Lei, W. Ke, C. Chen, Z. Chen, G. Yang and G. Fang, *Sol. RRL,* 2017, 1, 1700118.

S11 J.Peng, F. Kremer, D. Walter, Y. Wu, Y. Ji, J. Xiang, W. Liu, T. Duong, H. Shen, T. Lu, F. Brink, D. Zhong, L. Li, O. Lee, C. Lem, Y. Liu, K. Weber, T. White and K. Catchpole, *Nature*, 2022, 601, 573-578.

S12 Y. Zhao, T. Heumueller, J. Zhang, J. Luo, O. Kasian, S. Langner, C. Kupfer, B. Liu, Y. Zhong, J. Elia, A. Osvet, J. Wu, C. Liu, Z. Wan, C. Jia, N. Li, J. Hauch and C. Brabec, *Nat. Energy*, 2022, 7, 144-152.

S13 C. Liu, Y. Yang, K. Rakstys, A. Mahata, M. Franckevicius, E. Mosconi, R.

Skackauskaite, B. Ding, K. Brooks, O. Usiobo, J. Audinot, H. Kanda, S. Driukas, G. Kavaliauskaite, V. Gulbinas, M. Dessimoz, V.utas Getautis, F. Angelis, Y. Ding, S. Dai, P. Dyson and M. Nazeeruddin, *Nat. Commun.*, 2021, 12, 6394.